The Impact of Critical Operational Parameters on the Performance of the Aluminum Anode Baking Furnace

Abdul Raouf Tajik
Mem. ASME
Department of Aerospace Engineering,
Khalifa University,
P.O. Box 127788,
Abu Dhabi, UAE
e-mail: abdulraouf.tajik@ku.ac.ae

Tariq Shamim
Fellow ASME
Department of Mechanical Engineering,
Northern Illinois University,
DeKalb, IL 60115
e-mail: tshamim@niu.edu

Ahmed F. Ghoniem
Fellow ASME
Department of Mechanical Engineering,
Massachusetts Institute of Technology,
Cambridge, MA 02139
e-mail: ghoniem@mit.edu

Rashid K. Abu Al-Rub
Mem. ASME
Department of Mechanical Engineering,
Department of Aerospace Engineering,
Khalifa University,
P.O. Box 127788,
Abu Dhabi, UAE
e-mail: rashid.abualrub@ku.ac.ae

The Impact of Critical Operational Parameters on the Performance of the Aluminum Anode Baking Furnace

Minimizing energy consumption and reducing pollutant emissions during the carbon anode baking process are critically important for the aluminum industry. The present study investigates the effects of oxidizer inlet temperature, inlet oxygen concentration, equivalence ratio, refractory wall thermal conductivity, and refractory wall emissivity on the baking process using unsteady Reynolds-averaged Navier–Stokes (URANS)-based simulations in conjunction with the presumed probability density function method. Numerical results are combined with a response surface methodology (RSM) to optimize the anode baking process. The advantage of the coupled method is that it can adequately provide information on interactions of different input parameters. It is remarked that the significance level of the studied parameters varies drastically for different outputs. It is noted that diluting inlet oxygen concentration (from 23% in atmospheric air to 15%) at an elevated oxidizer temperature leads to enhanced furnace fuel efficiency, more uniform temperature distribution, and lower pollutant emissions. A linear model is detected to be adequate for response surface modeling of the anode baking furnace NO_x formation. On the other hand, furnace soot formation is modeled with a higher-order model due to the quadratic behavior of the response. [DOI: 10.1115/1.4048562]

Keywords: anode baking furnace, oxygen dilution, CFD, optimization, factorial design, response surface methodology, air emissions from fossil fuel combustion, energy conversion/systems, heat energy generation/storage/transfer

1 Introduction

The carbon anodes—which are baked at very high temperatures in massive furnaces (almost the size of a football field) for nearly 2 weeks—must be frequently replaced, as an approximately half a ton of carbon anode is consumed with each ton of aluminum produced, representing a significant financial and environmental expense. Non-uniform baking results in non-homogeneity in the anode properties, which is considered as one of the main reasons in the overconsumption of carbon anodes. As depicted in Fig. 1, carbon anodes should pass through several sections of preheating, firing, and cooling. It is imperative to ascertain that all the anodes experience almost identical temperature history to obtain a consistent evolution of material properties.

Anode baking furnaces have been widely studied numerically in the past two decades. In the anode baking furnace (ABF) process modeling, a simplistic approach is adopted. These models are sufficient for estimating the overall performance of the furnace [1–3]. However, it is incredibly challenging to employ ABF process models to perform transient turbulent combustion simulations. Anode baking furnace CFD modeling can provide a more suitable alternative in conducting detailed combustion modeling of these furnaces [4–8]. Severo et al. [9] reported the state-of-the-art technology on the baking of carbon anodes, and they presented several optimization studies. Tajik et al. [10–12] investigated the impact of flue-wall design modification on carbon anode baking uniformity. It was remarked that closing the baffle openings results in enhanced baking efficiency. Zaidani et al. [13–16] investigated the impact of deformed flue-wall on anode baking uniformity, and it was concluded that depending on the flue-wall deformation mode (a concave, a convex, and a combination of both), underbaking or overbaking of carbon anodes could occur.

Over the years, several studies are conducted to shed light on different clean combustion technologies to enhance the system's efficiency and to reduce pollutant emissions. Oxy-fuel combustion has attracted many researchers [17–21]. Moderate or Intense Low Oxygen Dilution (MILD) combustion is considered as one of the most promising clean combustion technologies [22–28]. MILD combustion outperforms the conventional combustion modes in terms of enhanced temperature uniformity since the chemical reactions occur in the entire combustion chamber, which consequences in enhanced uniformity of both temperature and species concentration. For MILD combustion, the inlet reactor temperature (T_{in}) is higher than the mixture self-ignition temperature (T_{si}). The maximum temperature increase (ΔT) for MILD combustion should be less than self-ignition temperature (T_{si}). Another essential condition for MILD combustion is that oxygen concentration inside the chamber is to be 3–13%.

The literature review suggests that the impact of different combustion modes on the performance of the anode baking furnaces is yet to be investigated. In the anode baking furnace, during the firing sections, the oxidizer is at an elevated temperature of 1100–1200 °C, which is higher than the self-ignition temperature of the fuel (see Fig. 1). Second, the inlet oxygen concentration is diluted as the flow passes the three firing sections in the fire direction. The inlet temperature and oxygen concentration differ from one section to the other, and this will affect the temperature and flow distributions. It is imperative to investigate the effect of oxygen concentration dilution at various preheating temperatures. It is also intended to study the effect of equivalence ratio to enhance the furnace fuel efficiency.

As shown in Fig. 2 [29], during the furnace service life, due to harsh thermal and mechanical environments, refractory wall

Contributed by the Advanced Energy Systems Division of ASME for publication in the Journal of Energy Resources Technology. Manuscript received April 6, 2020; final manuscript received September 10, 2020; published online October 14, 2020. Assoc. Editor: Tatiana Morosuk.

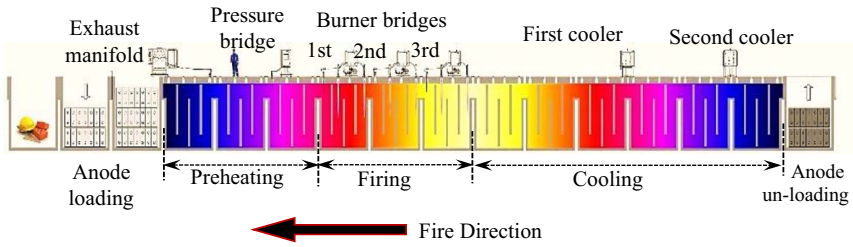

Fig. 1 The longitudinal view of a fire group

material properties deteriorate. During the firing section, radiation is the dominant mode of heat transfer, and thus, the refractory wall emissivity plays an important role. Moreover, anode baking furnaces are usually built of refractory materials of different thermal properties. Therefore, it is also crucial to study the effect of varying refractory thermal conductivity and emissivity. The impact of the above-mentioned five factors (i.e., oxygen concentration, inlet temperature, equivalence ratio, thermal conductivity, and emissivity of the refractory material) can be analyzed using the traditional one-factor-at-a-time (OFAT) approach. Nevertheless, instead, CFD simulations are combined with a response surface methodology (RSM) to investigate the effect of each parameter on the furnace performance comprehensively. The advantage of the coupled method over the traditional OFAT optimization approaches is that it can provide adequate information on interactions of different input variables. It can also effectively estimate the significance level of each factor and identify clear optimal settings of the variables. Using analysis of variance (ANOVA), the effect and significance level of each factor and their interactions are effectively estimated. Additionally, two and three response optimization is conducted. Finally, constraining some of the factors based on the furnace condition, multi-objective optimization of the anode baking process is carried out.

Thus, the current study aims at investigating the effect of mainstream inlet temperature (1150–1300 °C), mainstream inlet oxygen concentration (15–23.3%), equivalence ratio (0.25–0.125), refractory wall thermal conductivity (1.0–3.0 W/(m K)), and refractory wall emissivity (0.2–0.8). First, unsteady Reynolds-averaged Navier–Stokes (URANS)-based simulations equipped with the presumed probability density function (PDF) method are performed, and the results are compared with temperature measurements carried out in two anode baking furnaces. Second, CFD simulations are combined with an RSM to investigate the effect of each parameter on the furnace performance comprehensively. The results are assessed in terms of temperature distribution in both the gas side as well as the solid side, baking uniformity, and pollutant emissions.

Fig. 2 Deterioration of refractory materials properties due to aging effects [29]

2 Methodology

2.1 Computational Fluid Dynamics Model. Unsteady Reynolds-averaged Navier–Stokes-based simulations, in conjunction with the presumed probability density function method, are performed. The followings are the main governing equations solved to simulate confined turbulent non-premixed flames in anode baking furnaces. Transient continuity and conservation of momentum equations can be written as follows:

$$\frac{\partial \bar{\rho}}{\partial t} + \nabla \cdot (\bar{\rho}\tilde{\vec{v}}) = 0 \tag{1}$$

$$\frac{\partial (\bar{\rho}\tilde{\vec{v}})}{\partial t} + \nabla(\tilde{\vec{v}} \cdot \nabla\tilde{\vec{v}}) = -\nabla p + \nabla \cdot (\bar{\bar{\tau}}) + \bar{\rho}\mathbf{g} + \mathbf{F} \tag{2}$$

where $\bar{\bar{\tau}}$ is the stress tensor. A comprehensive study is carried out to study the sensitivity of the results to different RANS turbulence models, and it is remarked that the realizable $k-\varepsilon$ model provided the best corroboration with the experimental results. Thus, the realizable $k-\varepsilon$ model is employed for the closure of the conservation equations. The equations for turbulent kinetic energy (k) and its dissipation rate (ε) are as follows:

$$\frac{\partial (\bar{\rho}\tilde{k})}{\partial t} + \bar{\rho}(\tilde{\vec{v}} \cdot \nabla)\tilde{k} = \nabla \cdot \left[\left(\mu + \frac{\mu_t}{\sigma_k}\right)\nabla\tilde{k}\right] + G_k + G_b - \bar{\rho}\tilde{\varepsilon} - Y_M \tag{3}$$

$$\frac{\partial (\bar{\rho}\tilde{\varepsilon})}{\partial t} + \bar{\rho}(\tilde{\vec{v}} \cdot \nabla)\tilde{\varepsilon} = \nabla \cdot \left[\left(\mu + \frac{\mu_t}{\sigma_\varepsilon}\right)\nabla\tilde{\varepsilon}\right] + \rho C_1 S\tilde{\varepsilon} - \rho C_2 \frac{\tilde{\varepsilon}^2}{\tilde{k} + \sqrt{\nu\tilde{\varepsilon}}} + C_{1\varepsilon}\frac{\tilde{\varepsilon}}{\tilde{k}} C_{3\varepsilon} G_b \tag{4}$$

2.1.1 Combustion Modeling. The presumed PDF method has been widely used to simulate turbulent combustion with an excellent level of accuracy and affordable computational time for a wide range of engineering problems. Dong [30] used a RANS-based model equipped with a mixture fraction/pdf sub-model to conduct MILD combustion simulations. They remarked that the features of highly preheated air combustion could be successfully investigated employing the presumed PDF method. Graça et al. [31] conducted a comparative study on the effect of different turbulence chemistry interactions for MILD combustion modeling of a reverse flow small-scale combustor. They employed the realizable $k-\varepsilon$ as the turbulence model. They also remarked that the Eddy dissipation concept (EDC) and the presumed PDF model yields similar results for MILD combustion modeling. Galletti et al. [32], by using a β-function distributed PDF method, investigated the NO_x concentration distribution for MILD combustion burners.

Thus, in the present study, a β-function distributed PDF method is employed as the combustion model. The presumed PDF method is adopted to predict temperature field and species concentrations. The PDF must have a specific form in the form of two conserved scalar quantities known as the mixture fraction, f, and its variance, f'^2 [33,34]

$$\frac{\partial(\bar{\rho}\tilde{f})}{\partial t} + \nabla \cdot (\bar{\rho}\tilde{\vec{v}}\tilde{f}) = \nabla \cdot \left(\frac{\mu_t}{\sigma_t}\nabla\tilde{f}\right) \tag{5}$$

$$\frac{\partial(\bar{\rho}\widetilde{f'^2})}{\partial t} + \nabla \cdot (\bar{\rho}\tilde{\vec{v}}\widetilde{f'^2}) = \nabla \cdot \left(\frac{\mu_t}{\sigma_t}\nabla\widetilde{f'^2}\right) + C_g(\nabla\tilde{f})^2 - C_d\bar{\rho}\frac{\tilde{\varepsilon}}{\tilde{k}}\widetilde{f'^2} \tag{6}$$

where $f = Z_i - Z_{i,ox}/Z_{i,fuel} - Z_{i,ox}$ and $f' = f - \bar{f}$.

Direct numerical simulation (DNS) data indicated that the mixture fraction is beta-distributed [35,36]. Cao et al. [37] evaluated four types of presumed PDF models with large eddy simulation (LES) results, and they concluded that the β-function model performs good predictions for different flames. Kulkarni and Polifke [38] conducted LESs of autoignition in a turbulent hydrogen jet flame using a β-shape presumed PDF method. Hence, in the present study, the β-function PDF shape is adopted, which can be described by the following function of $\bar{f}$ and $\overline{f'^2}$:

$$p(f) = \frac{f^{\alpha-1}(1-f)^{\beta-1}}{\int f^{\alpha-1}(1-f)^{\beta-1}df} \tag{7}$$

where $\alpha = \bar{f}[\bar{f}(1-\bar{f})/\overline{f'^2} - 1]$ and $\beta = (1-\bar{f})[\bar{f}(1-\bar{f})/\overline{f'^2} - 1]$.

In non-adiabatic flows, the local thermochemical state also depends on the enthalpy H. Hence, a joint probability density function, $p(f, H)$, should be used due to the turbulent fluctuations. However, it is exceptionally challenging to compute $p(f, H)$ for most engineering applications. Henceforth, it is assumed that the enthalpy fluctuations are not dependent on the enthalpy level, and with this assumption, $p(f, H) = p(f)\delta(H - \bar{H})$ and mean scalars are calculated as follows:

$$\overline{\phi_i} = \int_0^1 \phi_i(f, \bar{H})p(f)df \tag{8}$$

In a non-adiabatic system, the determination of $\overline{\phi_i}$ thus requires the solution of the modeled transport equation for mean enthalpy

$$\frac{\partial(\bar{\rho}\bar{H})}{\partial t} + \nabla \cdot (\bar{\rho}\tilde{\vec{v}}\bar{H}) = \nabla \cdot \left(\frac{k_t}{c_p}\nabla\bar{H}\right) + S_h \tag{9}$$

The radiative transfer is mathematically described by the radiative transfer equation (RTE) for an absorbing, emitting, and scattering medium

$$\nabla \cdot (I_\lambda(\mathbf{r}, \mathbf{s})\mathbf{s}) = a_\lambda n^2 I_{b\lambda} - (a_\lambda + \sigma_s)I_\lambda(\mathbf{r}, \mathbf{s}) + \frac{\sigma_s}{4\pi}\int_0^{4\pi} I_\lambda(\mathbf{r}, \vec{s}')\phi(\mathbf{s}, \vec{s}')d\Omega' \tag{10}$$

where I_λ is the rate of variation of spectral radiation intensity at point r and direction s. The discrete ordinates (DO) method is used to solve the RTE. NO_x formation and reduction have been the research interest for several industrial applications [39–41]. Following is the transport equation for NO and other nitrogen-containing intermediate species required for thermal, prompt, and the fuel NO_x mechanisms:

$$\frac{\partial(\bar{\rho}\tilde{Y}_i)}{\partial t} + \nabla \cdot (\bar{\rho}\tilde{\vec{v}}\tilde{Y}_i) = \nabla \cdot (\bar{\rho}D\nabla\tilde{Y}_i) + S_i \tag{11}$$

where Y is the mass fraction, index i denotes NO, HCN, NH_3, and N_{2O} in the gas phase, and D is the effective diffusion coefficient. The source term S_i is to be determined by different NO_x mechanisms. The formation of thermal NO_x is expressed by a set of highly temperature-dependent chemical reactions known as the extended Zeldovich mechanism. For the sake of brevity, the principal reactions governing the formation of thermal, prompt, and fule NO_x are not detailed in the present section, and they can found in the ANSYS FLUENT theory manual.

In numerous experimental studies, the rate constants for these reactions have been measured, and the data obtained from these studies have been critically evaluated. The density-weighted time-averaged Navier–Stokes equations are considered for temperature, velocity, and species concentrations or mean mixture fraction and variance. To calculate NO level, a time-averaged NO formation rate must be computed at each point in the domain using the averaged flow-field information. In the NO_x model, a single- or joint-variable PDF regarding a normalized temperature, species mass fraction, or the combination of both is used to predict the NO_x emission. The mean turbulent reaction rate $\overline{w}$ can be described regarding the instantaneous rate w and a single or joint PDF of various variables [42]. In general

$$\overline{w} = \int\ldots\int w(V_1, V_1, \ldots)P(V_1, V_1, \ldots)dV_1dV_2\ldots \tag{12}$$

where V_1, V_1, … are temperature and/or the different species concentrations present. P is the probability density function. The PDF is used for weighting against the instantaneous rates of the production of NO and subsequent integration over suitable ranges to obtain the mean turbulent reaction rate. Hence, we have

$$\bar{S}_{NO} = \int\rho w_{NO}(V_1, V_1)P(V_1, V_1)dV_1dV_2 \tag{13}$$

where $\overline{S}_{NO}$ is the mean turbulent rate of production of NO, w_{NO} is the instantaneous rate of production given by, $P(V_1, V_2)$ are the PDFs of the variables V_1 and V_2. The same treatment applies to the HCN,NH_3, and N_{2O} source terms. Equation (13) must be integrated at every node and iteration. For a PDF in temperature, the limits of integration are determined from the minimum and maximum values of temperature in the combustion solution. For a PDF in mixture fraction, the limits of the integrations in Eq. (13) are determined from the values stored in the look-up tables.

It is commonly believed that the soot formation is due to the coagulation of polycyclic aromatic hydrocarbon (PAH) species. The Brookes–Moss soot prediction model has been initially developed for confined turbulent methane-air flames based one two transport equations, and the same model is adopted in the presented research. Following are the equations for the radical nuclei concentration and the soot mass fraction:

$$\frac{\partial(\bar{\rho}\tilde{Y}_{soot})}{\partial t} + \nabla \cdot (\bar{\rho}\tilde{\vec{v}}\tilde{Y}_{soot}) = \nabla \cdot \left(\frac{\mu_t}{\sigma_{soot}}\nabla\tilde{Y}_{soot}\right) + \frac{dM}{dt} \tag{14}$$

$$\frac{\partial(\bar{\rho}\tilde{b}^*_{nuc})}{\partial t} + \nabla \cdot (\bar{\rho}\tilde{\vec{v}}\tilde{b}^*_{nuc}) = \nabla \cdot \left(\frac{\mu_t}{\sigma_{nuc}}\nabla\tilde{b}^*_{nuc}\right) + \frac{1}{N_{norm}}\frac{dN}{dt} \tag{15}$$

Equation (16) expresses the soot particles instantaneous production exposed to coagulation in the free molecular regime and nucleation from the gas phase

$$\frac{dN}{dt} = \underbrace{C_\alpha N_A\left(\frac{X_{prec}P}{RT}\right)^l \exp\left(-\frac{T_\alpha}{T}\right)}_{Nucleation} - \underbrace{C_\beta\left(\frac{24RT}{\rho_{soot}N_A}\right)^{\frac{1}{2}} d_p^{\frac{1}{2}}N^2}_{Coagulation} \tag{16}$$

The local acetylene concentration for methane is proportional to the nucleation rate for soot particles. The following expression

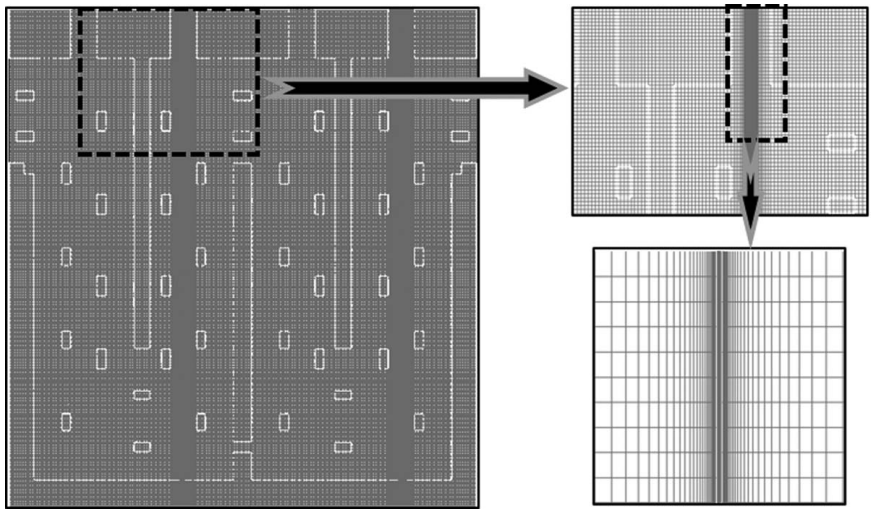

Fig. 3 Generated structured computational grids (minimum orthogonal quality = 1.0 and maximum ortho skew = 0)

Table 1 Grid independence tests for spatial grids and temporal grids

Spatial grids				Temporal grids			
Grid size	66,568	266,272	1,065,088	Time-step (s)	100	10	1
$T_{gas-avg}$ (°C)	1232	1230	1228	$T_{gas-avg}$ (°C)	1232	1231	1228
O_{2-avg} (%)	12.23	12.21	12.18	O_{2-avg} (%)	12.23	12.22	12.22
CO_{2-avg}(ppm)	830	810	800	CO_{2-avg}(ppm)	830	820	815

models the source term for soot mass concentration:

$$\frac{dM}{dt} = \underbrace{M_P C_\alpha \left(\frac{X_{prec}P}{RT}\right)^l \exp\left(-\frac{T_\alpha}{T}\right)}_{Nucleation} - \underbrace{C_{oxid} C_\omega \eta_{coll} \left(\frac{X_{OH}P}{RT}\right) \sqrt{T}(\pi N)^{\frac{1}{3}} \left(\frac{6M}{\rho_{soot}}\right)^{\frac{2}{3}}}_{Oxidation} + \underbrace{C_\gamma \left(\frac{X_{prec}P}{RT}\right)^m \exp\left(-\frac{T_\gamma}{T}\right) \left[(\pi N)^{\frac{1}{3}} \left(\frac{6M}{\rho_{soot}}\right)^{\frac{2}{3}}\right]^n}_{Surface\ Growth} \quad (17)$$

The model constants are C_γ, C_{oxid}, C_w, m, and n. The mass of an incipient soot particle is $M_P = 144$ kg/(kg mol). The Brookes–Moss model was initially proposed for non-premixed confined methane flame jets and hence can be suitably used for the present study.

2.1.2 Numerical Implementation. Figure 3 depicts the structured computational grid. It is noteworthy that the flue-wall geometry used in the present study represents a state-of-the-art flue-wall design that is being used in the aluminum industry, and no geometric simplification is applied. The CFD software (FLUENT 19.2) is used to perform URANS-based simulations. The approach is based on finite volume discretization. The transient formulation is done based on the second-order fully implicit method, and the second-order upwind scheme is used for the spatial discretization. Table 1 summarizes spatial and temporal grids independence tests (GIT). Gas temperature and species concentrations are monitored, and it is remarked that the results are grid-independent. The time-step size is reduced from 100 s to 1 s, and the difference is noticed to be less than 0.5%. The simulations are initialized with a time-step of 0.01 s, and afterward, the time-step increased gradually to ensure complete convergence. The residuals for all the equations are set to 10^{-6} as the absolute criteria for convergence. The number of iterations is set to 60 for each time-step, ensuring a complete convergence for each time-step.

2.2 Coupling Numerical Results With a Response Surface Methodology. In the literature, numerous studies are reported on combing CFD simulations with response surface methodologies for optimizing purposes. For instance, to maximize the methane production from bituminous coal through gasification, Zhang et al. [43] examined the effect of 12 parameters, out of which four factors were found to be statistically significant. They performed a two-level factorial design. Performing a parametric statistical experimental design study, Thummakul et al. [44] used the design of experiment (DOE) techniques to investigate how variation in four factors affects the CO_2 capture efficiency in a fluidized bed. Naqiuddin et al. [45] conducted a numerical investigation in optimizing the segmented micro-channel heat sink using a design of experiment technique named the Taguchi–Grey method. Performing 27 CFD simulations, they investigated the effect of six parameters on three responses. Shirvan et al. [46], using numerical simulations and response surface methodology, identified the optimum geometrical parameters of a solar updraft tower to maximize the power output. Bahai et al. [47] used a factorial design analysis to study the impact of geometry in drill string screw connectors.

Thus, CFD simulations results are combined with a response surface methodology to optimize the anode baking process single and multi-objectively. The effects of five vital furnace operational-physical parameters are systematically investigated. All possible combinations of the input parameters are tested. In doing so, a design of experiment technique named factorial design is considered. For two-level full factorial design, the real values for five factors are coded by setting "+1," "0," and "−1" for the lower, middle, and higher levels—a total of 33 CFD simulations, 32 corner simulations, and one center point.

Table 2 Real values for higher and lower levels of the five factors

	$Y_{O_2-inlet}$(%)	T_{inlet} (°C)	ϕ(–)	k(W/m K)	ε_w(–)
Lower-level (Coded value = −1.0)	15.0	1150	0.125	1.0	0.2
Higher-level (Coded value = +1.0)	23.3	1300	0.250	3.0	0.8

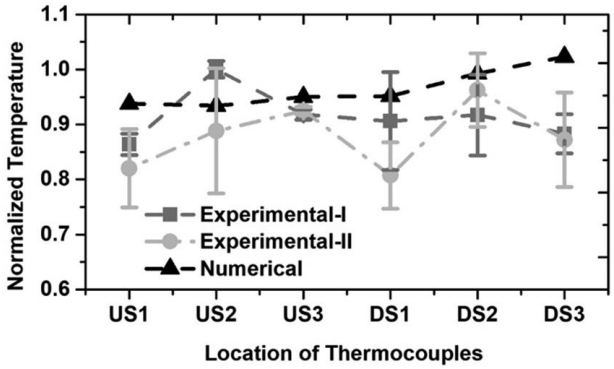

Fig. 4 Model's validation with the experimental measurements (EGA)

For mainstream inlet oxygen concentration ($Y_{O_2-Inlet}$), the higher-level is considered as 23.3%, which is the oxygen concentration in the air, and the lower-level value is chosen as 15%. The concentration should not reduce further since the extreme decrement in mainstream inlet oxygen concentration in the firing section leads to increased incomplete combustion and extra soot formation in the preheating sections since the sections are one after the other. The lower and higher values of mainstream stream inlet temperature (T_{inlet}) are chosen to be 1150 °C and 1300 °C, which are the standard operating conditions to achieve complete anode carbonization.

The maximum reaction temperature can be achieved for an equivalence ratio equal to unity. Nonetheless, in the case of the anode baking process, enhancing anode baking uniformity is imperative. In a previous study by our group [10], it is remarked that by the decrease in equivalence ratio, the reactions occur more homogenously and in a larger volume of the flue-wall, which is very critical for enhancing anode baking uniformity. Thus, lower and higher-level for the equivalence ratio (ϕ) are chosen to be 0.125 and 0.250.

In the market, depending on the price, refractory wall thermal conductivity (k) can vary between 1.0 and 3.0 W/(m K), and hence, these values are considered as lower and higher values. The emissivity (ε_w) of the refractory wall for a new anode baking furnace is approximately 0.8. For an old anode baking furnace, it can reduce to 0.2, and therefore, the lower and higher values for the emissivity are chosen to be 0.2 and 0.8, respectively. Table 2 summarizes the real values for higher and lower levels of all the variables. Additionally, the detailed description of the response surface methodology is provided in the Appendix.

2.3 Computational Fluid Dynamics Model Validation. The numerical model is comprehensively validated by comparing the results with the experimental measurements taken from two different flue-walls at Emirates Global Aluminum (EGA), UAE. The flue-gas temperature distribution experiences a high non-uniformity level. Thus, the thermocouples are located at different flue-wall heights in upstream (US) and downstream (DS) of the flow. DS_1, DS_2, and DS_3 are referred to the thermocouples mounted at the bottom, middle, and top of the flue-wall in downstream of the flow and likewise for US_1, US_2, and US_3 in the flow upstream. The error bars of 1.5 standard deviations depict the variation in the measurement results. As shown in Fig. 4, there is a good match between the numerical results with their counterpart experimental measurements. For DS_3, the numerical result overpredicts the experimental measurements since there is a loss in the gas temperature at the flow downstream due to occasional headwall openings, and this effect is not incorporated into the model.

Till the date, no measurements on flame temperature and species concentrations are reported in the case of the anode baking furnace. Therefore, due to a lack of experimental data on flame temperature and species concentrations of non-premixed combustion in the case of the anode baking furnace, the numerical model used in the present study is further validated with the experimental work carried out by Brookes and Moss [48] on a different geometry. The NO_x results are verified with the numerical results reported by Yang et al. [49]. Figure 5 shows the model's validation with the reported data. There is an excellent match between the reported data and the results from the present study.

3 Results and Discussions

Section 3.1 discusses the effects of five parameters on the furnace heat transfer characteristics. Section 3.2 studies the impact of parameters on CO, NO_x, and soot formations. In Sec. 3.3,

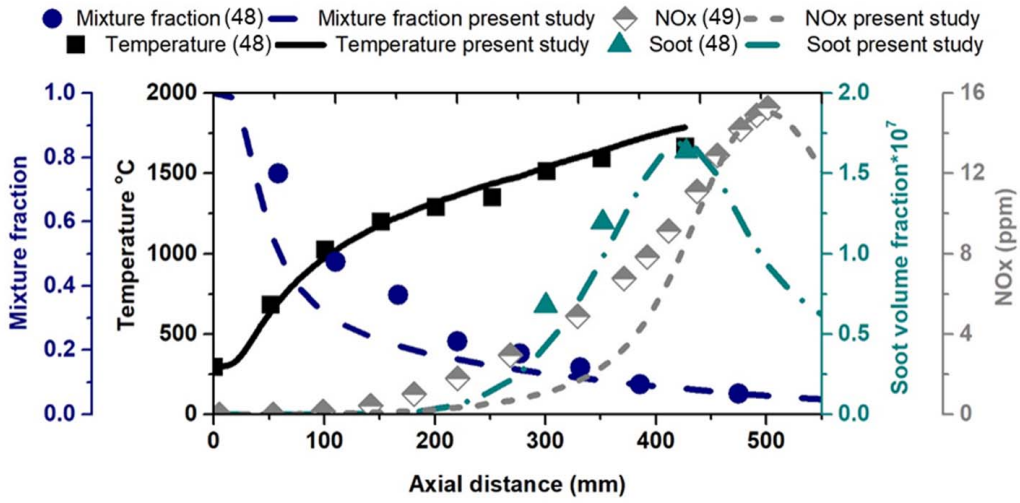

Fig. 5 Model's validation with the reported data [48,49]

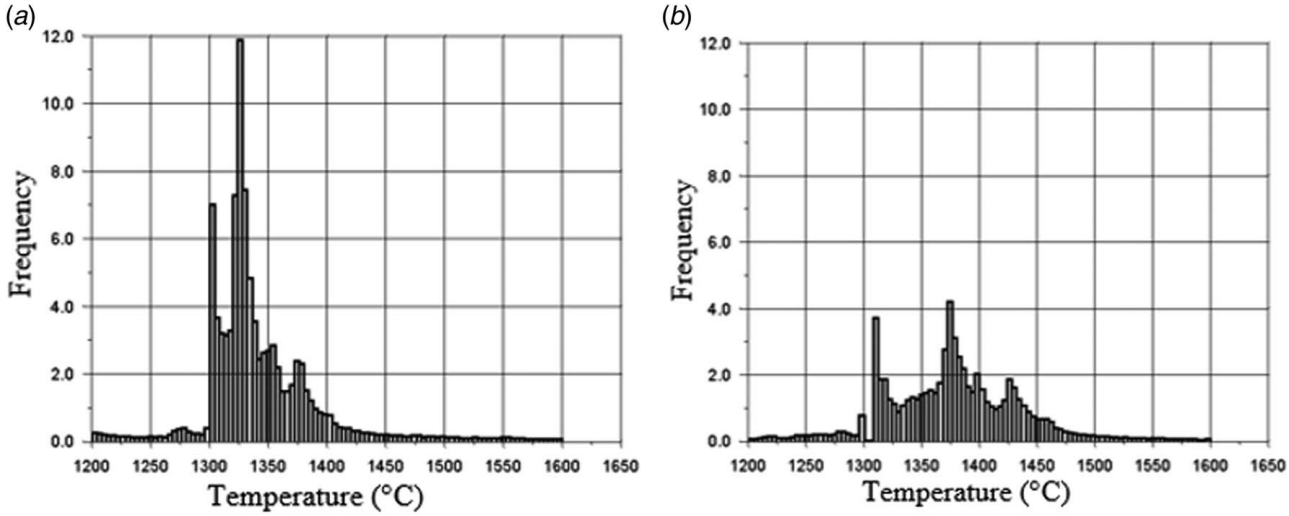

Fig. 6 Temperature histograms (°C) for (*a*) Run 31 ($Y_{O_2} = 23.3\%$) and (*b*) Run 32 ($Y_{O_2} = 15.0\%$)

we address the effects of parameters on multiple outputs simultaneously.

3.1 Heat Transfer Characteristics. In this section, we discuss the effects of five parameters on the furnace heat transfer characteristics. Figure 6 shows the temperature histograms (°C) for varying inlet oxygen concentrations for two cases; Run-31 and Run-32, with the inlet oxygen concentration of 15% and 23.3%, respectively. As can be seen, the horizontal spread for Run-32 ($Y_{O_2-inlet} = 23.3\%$) indicates a higher temperature variation, and it can be observed that for Run-31 ($Y_{O_2-inlet} = 15\%$), the temperature is more uniform, in the range of 1300–1400 °C, which consequences in an enhanced baking uniformity since the chemical reactions take place in a larger volume of the flue-wall cavity and the uniformity of both temperature and the chemical species concentration is enhanced. For an inlet oxygen concentration of 15%, ΔT is significantly lower than T_{si}, and this is one of the main features of MILD combustion, as pointed out earlier. It is noteworthy that oxygen dilution can be easily implemented since anode baking furnaces are circular kilns analogous to a closed chain connected through crossovers at the two extremes. The exhaust gases can be recirculated through anode baking furnace crossovers, which dilute inlet oxygen concentration that eventually results in higher fuel efficiency and lowers pollutant emissions.

Figure 7 provides values for average temperature (°C) in the gas domain, solid domain, and the whole computational domain for all the runs. There is an ascending trend for the first 16 runs, which

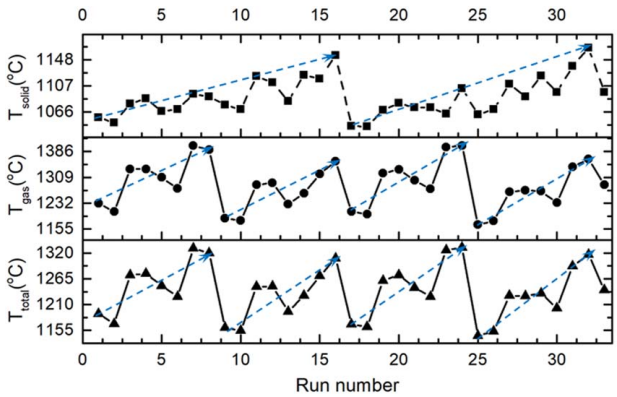

Fig. 7 Average temperature (°C) (gas domain, solid domain, and total domain) for all the runs

indicates a significant effect of wall emissivity on solids temperature. For gas temperature as a response, the shift in mean occurs every eight runs. The total temperature behaves similarly to the gas temperature. Figure 8 demonstrates the temperature standard deviation (°C) and uniformity index (UI) for the solid, gas, and the whole computational domain. A similar interpretation as that of Fig. 8 can be obtained for the standard deviation and uniformity index plots. It is also apparent that the standard deviation and uniformity index behave oppositely.

3.1.1 Analysis of Variance. To examine if the change in one of the levels or their interaction is significant, we need to perform a hypothesis test for the average response using ANOVA techniques. Figure 9 depicts the Pareto chart of the standardized effects on the gas and the solid temperature. The backward elimination method is used to identify the significant factors. Initially, the model includes all the possible terms in the model and removes the least significant terms for each step. The convergence is completed when all the factors in the model (the main effects and their interactions) have *p*-values less than or equal to the stated Alpha (α). The α value is considered to be 0.1. Based on Lenth's analysis, the reference line is drawn based on the median of the effects. The standardized effect of more than 1.7 is considered to be significant. It can be observed that the mainstream inlet temperature is the most significant factor when the gas temperature is the output. On the contrary, when the solid temperature is chosen as an output, refractory thermal conductivity is found to be the most significant factor.

Figure 10 depicts the normal plots of the effects for gas temperature uniformity index and gas temperature standard deviation. Factors "*B*," "*C*," and "*D*" are the most significant factors. It can also be noticed that the "*C*" and "*D*" are on the two different sides, which indicate "*D*" is inversely proportional to the baking uniformity. The equivalence ratio, followed by the mainstream oxygen concentration are the most significant factors. It is interesting to note that the normal plots are a mirror image of each other for the standard deviation and uniformity index.

3.2 Emissions Characteristics. In this section, we study the impact of the studied parameters on CO, NO_x, and soot formations. Average O_2 concentration behaves in a sinusoidal manner with a shift in the mean value every four runs. This indicates that the inlet oxygen concentration has the most significant effect in combination with the equivalence ratio, which alters every four runs. CO concentration wavers between a minimum and maximum, which indicates a strong relation between CO concentration and the change in inlet oxygen concentration. For NO_x formation, there is

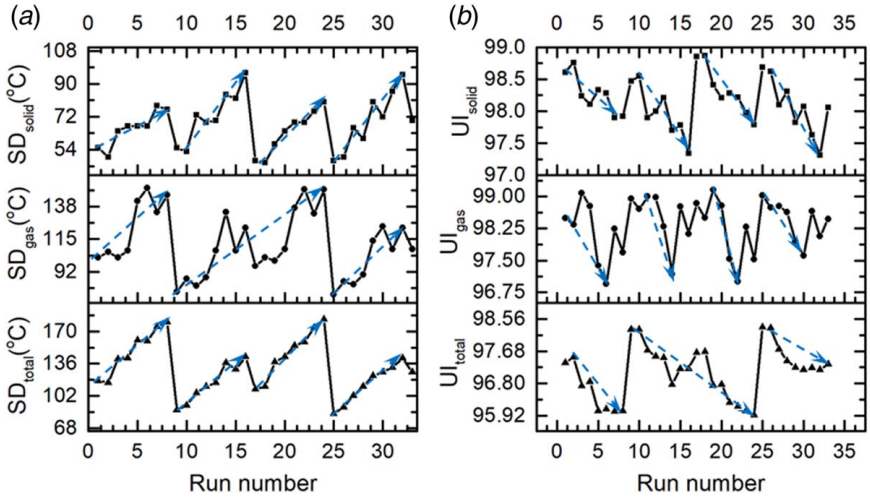

Fig. 8 (*a*) Temperature standard deviation (°C) and (*b*) uniformity index (gas domain, solid domain, and total domain) for all the runs

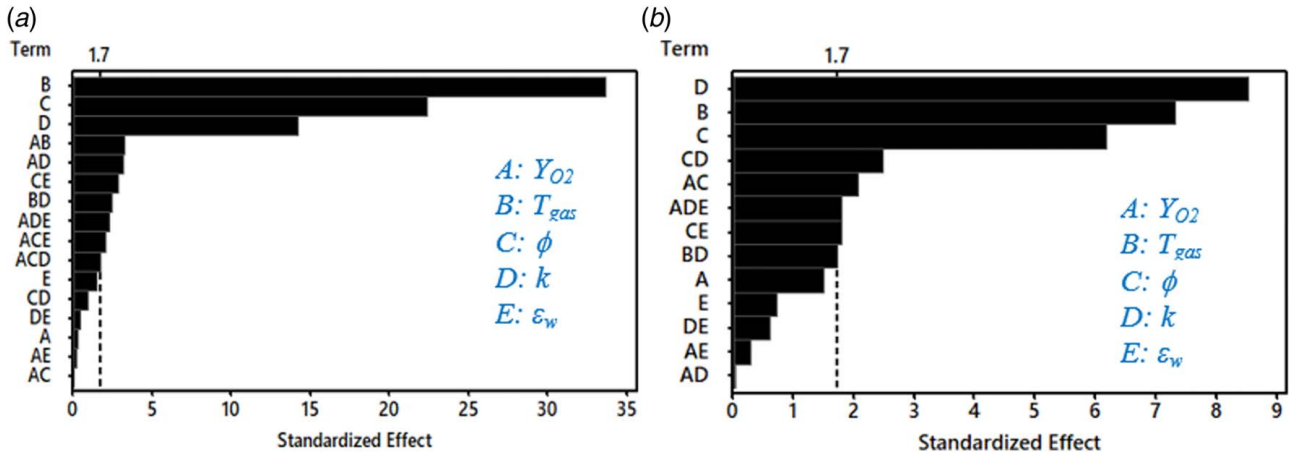

Fig. 9 Pareto chart of the standardized effects on (*a*) average gas temperature and (*b*) average solid temperature

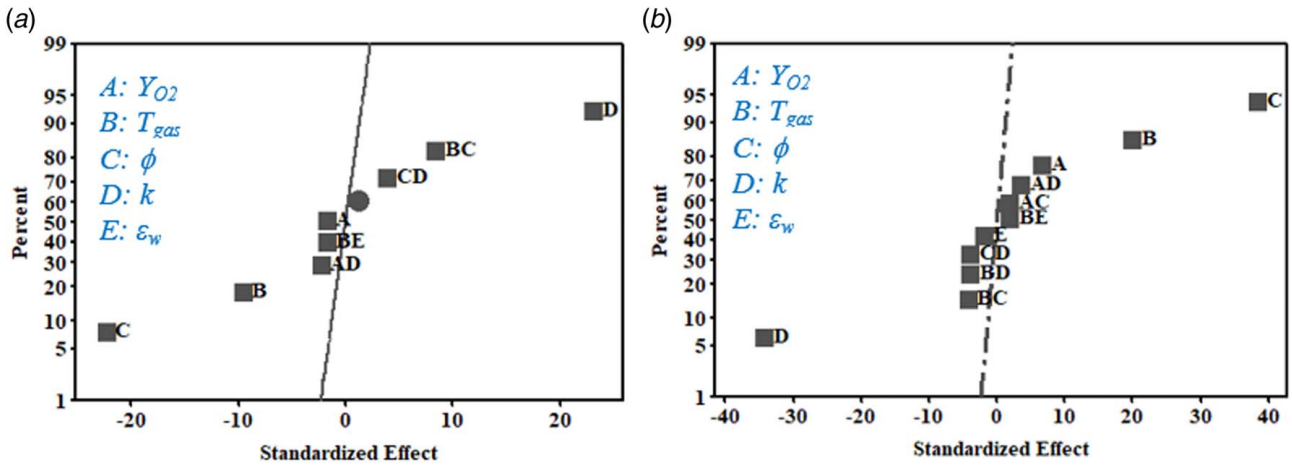

Fig. 10 Normal plots of the effects on (*a*) gas temperature uniformity index and (*b*) gas temperature standard deviation

a substantial shift in the mean values every eight runs, which are in agreement with the change in thermal conductivity, which is very unlikely. Hence, for NO_x, a combination of factors affects the result, which will be discussed in Sec. 3.2.1. Regarding the soot formation, there is no evident pattern as a function of the number of runs. A random order occurs, which indicates that a linear model would be insufficient to predict soot in anode baking furnaces, and higher-order mode to be considered.

3.2.1 Analysis of Variance. In this section, through ANOVA, we examine if the alteration in one of the levels or their interaction is significant. Figure 11 depicts the Pareto charts and contour plots

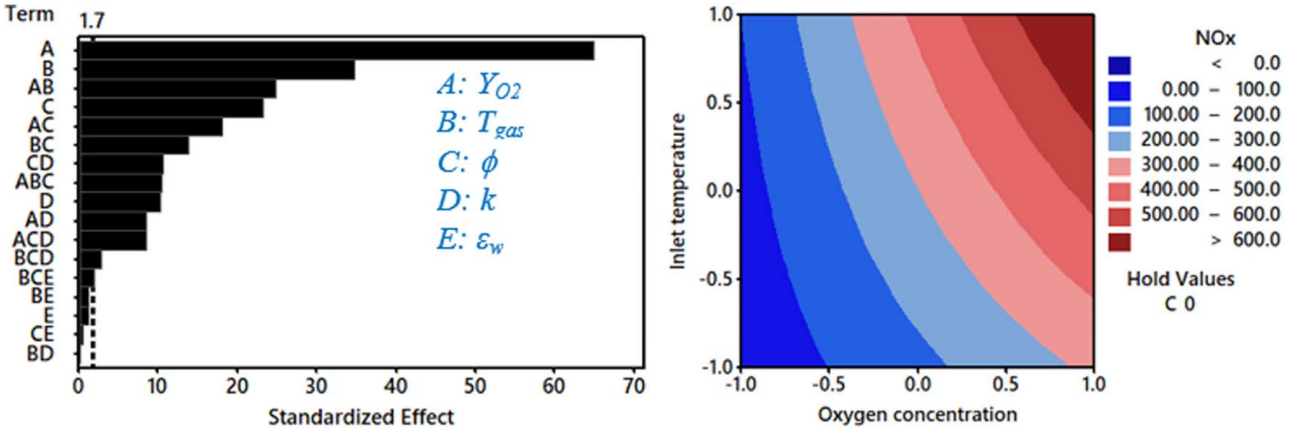

Fig. 11 Pareto chart and response surface plot for NO_x concentration (ppm)

of NO_x concentration. For each contour, the other factors are held at "zero," as mentioned in the legend. It can be perceived that the inlet oxygen concentration ("*A*") is the most significant factor in NO_x formation, followed by the equivalence ratio ("*B*") and their interaction ("*AB*"). The contour plot also confirms the same interpretation, i.e., the gas temperature is reduced in the case of diluted oxygen concentration, and as a result, the molecular nitrogen (N_2) and oxygen (O_2) disassociate less at a lower temperature. Thus, the thermal NO_x and ultimately overall NO_x concentration decrease drastically by oxygen dilution. It should be noted that the combustion products from burner bridge 3 (BB_3) will be the mainstream oxidizer for the next two preheating sections (PH_2, PH_2), where the volatile gasses combustion occurs. It is also apparent from the contour plot in Fig. 11 that the quadratic effect is not significant, and NO_x formation can be modeled as a linear model.

Table 3 provides the ANOVA parameters for NO_x and soot concentration. Factors "*A*," "*B*," "*D*," and "*E*" are the significant main effects, and "*AB*," "*AD*," and "*BE*" are the significant two-way interactions effects, and the curvature effect is not substantial. Hence, for NO_x, the model is considered to be linear. On the contrary, in part-b, the curvature effect for the soot concentration is significant, and the quadratic terms must be included for soot concentration as a response. In the case of soot formation, factors "*A*" and "*C*" and their interaction ("*AC*") are identified to be significant. As shown in Fig. 12, the quadratic effect is evident from the contour plots. A lower oxygen concentration gives rise to a lower temperature, and this consequences in delayed soot inception, and hence, an average soot mass fraction decrease. However, it can be observed that at higher oxygen concentration and equivalence ratio, the soot formation reduces. This is an essential observation for choosing acceptable furnace operational conditions.

3.3 Multi-Objective Optimization. In the anode baking process, often it is required to optimize multiple outputs simultaneously. The ultimate aim of the anode baking process optimization is to meet a target gas temperature, and at the same time to maximize the uniformity, to minimize fuel consumption, and to minimize pollutant emissions. The responses are divided into three categories, namely, (1) temperature values, (2) baking uniformity values, and (3) species concentration values.

Using 2D overlaid contour plots, the optimized setting of significant operational parameters for two and three response are spotted. The outputs are NO_x concentration (ppm), soot volume fraction, and gas temperature (°C). Figure 13 illustrates the optimization results for three different cases. In case-a, NO_x concentration (ppm) is constrained to a maximum of 300 ppm and gas temperature to be between 1260 °C and 1310 °C while holding the other three factors at "0." The optimized operating range for factors "*A*" and "*B*" are approximated as follows: $-1.0 < A < 0.4$ and $-0.6 < B < 0.5$. For case-b, the optimized range of soot volume fraction is set to 10^{-7}–10^{-6}, and the gas temperature to be similar to case-a (between 1260 °C and 1310 °C) while holding the other three factors at "0." The optimized operating range for factors "*A*" and "*C*" are approximated to be $-1.0 < A < 1.0$ and $-0.3 < C < 0.7$. Similarly, it can be perceived that at higher oxygen concentration ("*A*" = 1.0) combined with the equivalence ratio of ("*C*" = 0.4–0.7), soot formation reduces. This area can also be considered as the optimized furnace operational condition. In Figure 13, case-c depicts a combination of cases-a and case-b. The optimized operating range for factors "*A*" and "*C*" are approximated to be $-1.0 < A < -0.5$ and $-0.3 < C < 0.7$.

Table 3 ANOVA table for (*a*) NO_x (ppm) and (*b*) soot volume fraction

(*a*)

Source	DF	*F*-value	*P*-value
Model	9	83.93	0.000
Linear	4	155	0.000
A	1	431	0.000
B	1	123	0.000
C	1	55	0.000
D	1	10.8	0.003
2-Way	5	26.8	0.000
*A***B*	1	63	0.000
*A***C*	1	33	0.000
*A***D*	1	7.3	0.013
*B***C*	1	19.	0.000
*C***D*	1	11.4	0.003
Error	23	–	–
Curvature	1	2.1	0.158
Total	32	–	–

(*b*)

Source	DF	*F*-value	*P*-value
Model	11	205	0.000
Linear	5	374	0.000
A	1	1301	0.000
B	1	69	0.000
C	1	500	0.000
D	1	0.00	0.972
E	1	0.03	0.854
2-Way	5	72.9	0.000
*A***B*	1	4.9	0.038
*A***C*	1	314	0.000
*A***D*	1	26.9	0.000
*B***C*	1	5.9	0.024
*C***D*	1	12.5	0.002
Curvature	1	20.9	0.000
Error	21	–	–
Total	32	–	–

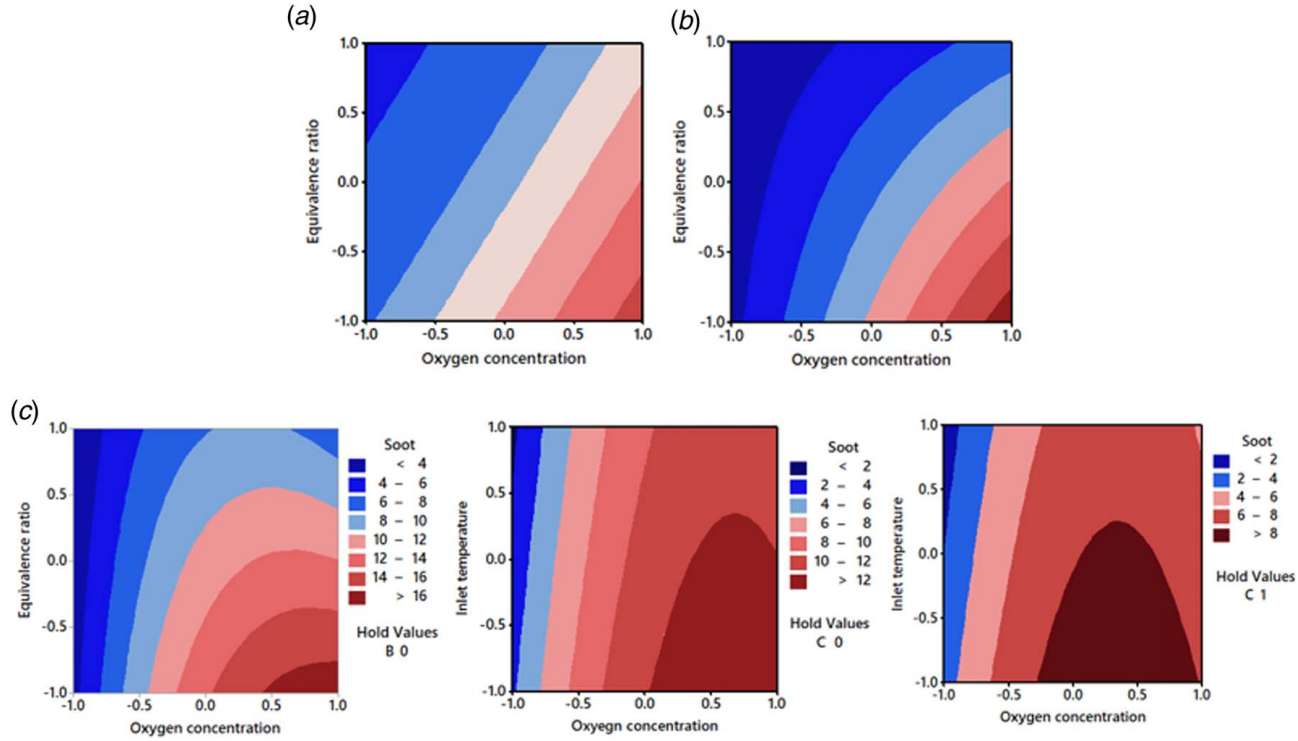

Fig. 12 Soot volume fraction $\times 10^7$: (*a*) the main effects only, (*b*) interactions included, and (*c*) quadratic effects included

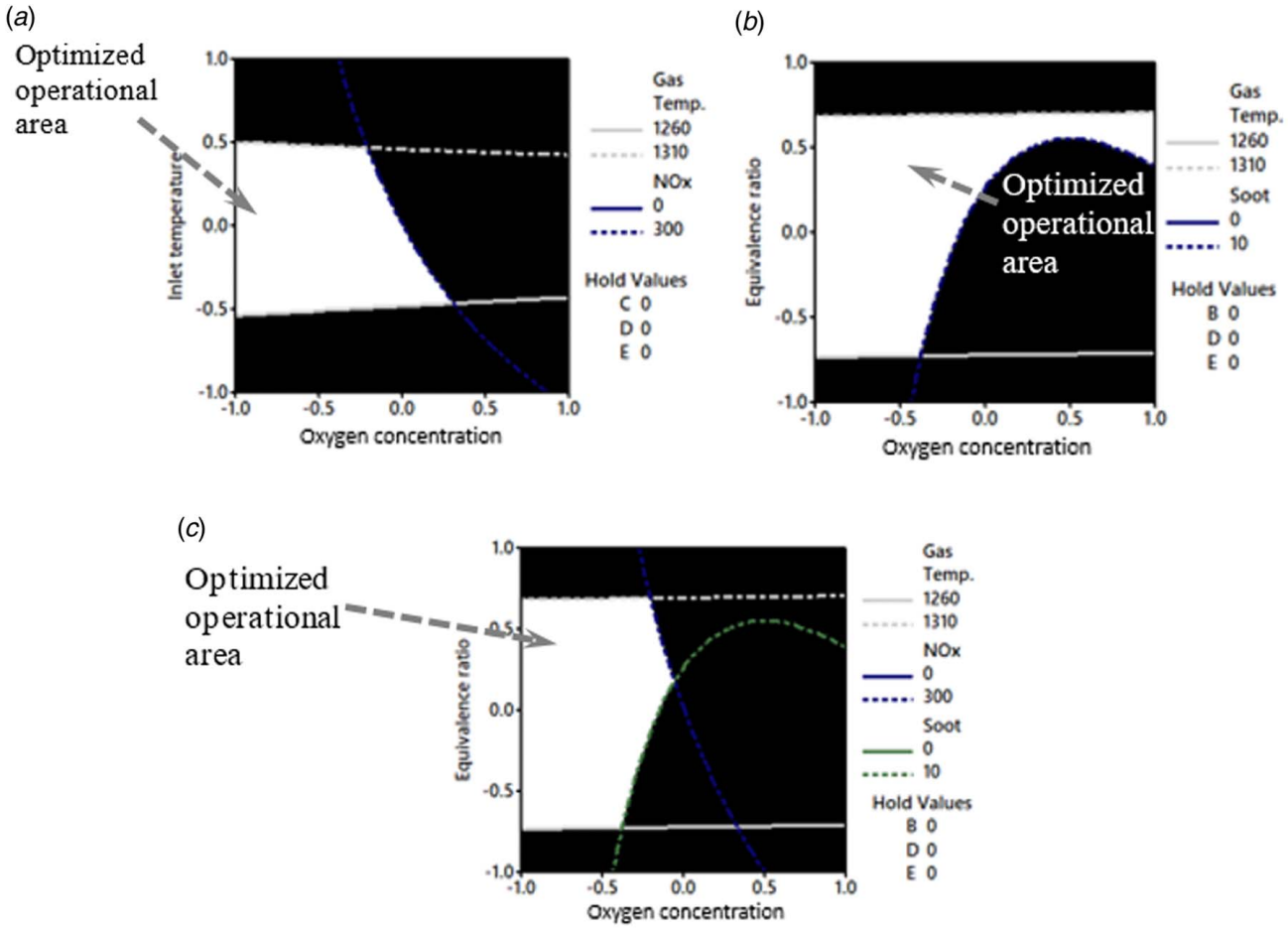

Fig. 13 Two and three objectives optimization cases: (*a*) NO_x (ppm) and gas temperature (°C), (*b*) soot volume fraction and gas temperature (°C), and (c) NO_x (ppm), soot volume fraction, and gas temperature (°C)

Table 4 Sum of square approach for the ANOVA test

Equation	Description
$\bar{y}_i = \frac{1}{bn}\sum_{j=1}^{b}\sum_{k=1}^{n} y_{ijk}$	Responses from changes in "*A*" at "*a*" different levels averaged over "*b*" and "*n*" (average effect of input "*A*")
$\bar{y}_j = \frac{1}{an}\sum_{i=1}^{a}\sum_{k=1}^{n} y_{ijk}$	Responses from changes in "*B*" at *b* different levels averaged over "*a*" and "*n*" (average effect of input "*B*")
$\bar{y}_{ij} = \frac{1}{n}\sum_{k=1}^{n} y_{ijk}$	Responses from changes in "*A*" and "*B*" at ab levels averaged overall "*n*" (average effect of "*AB*")
$\bar{\bar{y}} = \frac{1}{abn}\sum_{i=1}^{a}\sum_{j=1}^{b}\sum_{k=1}^{n} y_{ijk}$	The average response for all levels (grand mean)

Table 5 ANOVA table for a full factorial design (two factors *A* and *B*)

Source of variation	Sum of squares	Degrees-of-freedom	Mean squares	F	F_0
A	SS_A	$a-1$	$MS_A = SS_A/(a-1)$	$F = MS_A/MS_E$	$F_{(1-\alpha),a-1,ab(n-1)}$
B	SS_B	$b-1$	$MS_B = SS_B/(b-1)$	$F = MS_B/MS_E$	$F_{(1-\alpha),b-1,ab(n-1)}$
AB	SS_{AB}	$(a-1)(b-1)$	$MS_{AB} = SS_{AB}/(a-1)(b-1)$	$F = MS_{AB}/MS_E$	$F_{(1-\alpha),(a-1)(b-1),ab(n-1)}$
Error	SS_E	$ab(n-1)$	$MS_E = SS_E/ab(n-1)$		
Total	SS_T	$abn-1$	*NB: For a 2-level factorial design, $a = b = 2$. Thus, d.o.f = 1 for each term.*		

For the anode baking process, the practicalities must be considered while performing multi-objective optimization. Considering flue-wall material properties and furnace aging status, the values for k and ε_w should be fixed. The equivalence ratio or fuel consumption can be held within a range or set to minimization based on the required productivity. The furnace productivity is the deciding factor on how high/low the average target gas temperature should be fixed. Typically, there are constraints over one or more number of factors based on flue-wall material properties and age of the furnace. Multi-objective optimization of the anode baking process is performed while constraining some of the furnace's physical properties, such as factors "*D*" and "*E*." It is aimed to minimize NO_x, soot, and CO emissions while meeting a target gas temperature of 1250 °C, the UI is targeted to be maximized while factors "*D*" and "*E*" are held at "−0.5" and "0.5." The optimal settings of factors "*A*," "*B*," and "*C*" are found to be −1.0, −0.21, and −1.0. Composite desirability ("*CD*") is defined as a parameter to evaluate how the optimized settings meet the overall objective. *CD* varies from zero to one where unity represents the ideal case, and nil means that one or more responses are outside their acceptable limits. The *CD* value, in this case, is 0.94, which shows that the optimal settings of the factors are satisfactory.

4 Conclusions

The present study addresses the effects of mainstream inlet temperature, mainstream inlet oxygen concentration, equivalence ratio, refractory wall thermal conductivity, and refractory wall emissivity on heat transfer, combustion, and emissions characteristics of anode baking furnaces for the aluminum production. URANS-based simulations are performed in conjunction with the presumed PDF method. CFD simulations are combined with a response surface methodology to optimize the anode baking process.

It is remarked that lower inlet oxygen concentration ($Y_{O_2-inlet} = 15.0\%$) results in enhanced performance of the anode baking, which results in higher energy efficiency and drastically lower pollutant emission. The reason is that the maximum flame temperature reduces, and reactions occur more homogeneously and in a larger volume of the anode baking furnace. This is a significant observation since anode baking furnaces are circular analogous to a closed chain connected through crossovers at the two extremes. Using this circular geometrical property, the exhaust gases can be recirculated through anode baking furnace crossovers, which dilute inlet oxygen concentration that eventually results in higher fuel efficiency and lowers pollutant emissions. It has been depicted that the significance level of the input parameters varies drastically for different outputs (response). The refractory thermal conductivity and mainstream inlet temperature are statistically the most significant factors for solid and gas temperatures, respectively. Mainstream inlet oxygen concentration has the highest impact on anode baking furnace CO formation. The anode baking furnace NO_x formation is affected significantly by the inlet oxygen concentration and temperature, and a linear model is confirmed to be adequate for its response surface model. In contrast, the furnace soot formation is modeled with a higher-order model due to the quadratic behavior of the response. Multi-objective optimization is carried out for several scenarios with and without constraining the factors. Coupling anode baking furnace CFD simulations results with the response surface methodologies demonstrated great potential in the optimization of the anode baking process with enhanced energy efficiency and baking uniformity, which is a necessity for the sustainable production of the aluminum.

Acknowledgment

The authors acknowledge the financial support provided by the Emirates Global Aluminum (EGA) in the UAE under the direction of Dr. Mohamed O. Mahmoud. Also, the authors acknowledge the support and help of the carbon anode team at EGA.

Conflict of Interest

There are no conflicts of interest.

Data Availability Statement

The datasets generated and supporting the findings of this article are obtainable from the corresponding author upon reasonable request. The authors attest that all data for this study are included in the paper. Data provided by a third party are listed in Acknowledgment. No data, models, or code were generated or used for this paper.

Nomenclature

a = absorption coefficient
f = mixture fraction
k = turbulent kinetic energy
n = the refractive index
p = the static pressure
C = the linear anisotropic phase function coefficient
E = the total energy
G = incident radiation
H = enthalpy
I = the unit tensor
M = soot mass concentration
N = soot particle number density
S = $\sqrt{2S_{ij}S_{ji}}$ where $S_{ij} = 1/2(\partial u_j/\partial u_i + \partial u_i/\partial u_j)$
$\mathbf{F}$ = external body force
h_j = the mixture enthalpy
k_{eff} = effective thermal conductivity
k_t = turbulent thermal conductivity
C_1 = max[0.43, $\eta/\eta+5$] where $\eta = Sk/\varepsilon$
C_p = the mixture specific heat
$D_{i,m}$ = the mass diffusion coefficient of ith species
D_t = turbulent diffusivity
G_b = generation of turbulence kinetic energy due to buoyancy
G_k = generation of turbulence kinetic energy due to the mean velocity gradients
$I_{b\lambda}$ = the blackbody intensity given by the Planck function
I_{ri} = the radiative intensity
M_p = mass of an incipient soot particle
N_{norm} = 10^{15} particles
$R_{i,j}$ = the reaction rate
S_h = source term due to radiation, and heat transfer to wall boundaries
T_{si} = self-ignition temperature
X_{sgs} = mole fraction of the participating surface growth species
Y_M = the contribution of the fluctuating dilatation in compressible turbulence to the overall dissipation rate
Y_{soot} = soot mass fraction
$\mathbf{J}_i$ = the mass diffusion flux of the jth species
f' = the variance of mixture fraction equals to $f - \bar{f}$
$\vec{v}$ = velocity vector
b^*_{nuc} = normalized radical nuclei concentration
$C_{1\varepsilon}$ and C_2 = constants
C_d and C_g = constants for the presumed PDF method
C_α and C_β = Moss–Brookes model constant
C_γ, C_{oxid}, C_ω, m, and n = additional constants for Moss–Brookes for estimating source term of soot mass concentration
Sc_t = turbulent Schmidt number
Y_{pr},Y_{fu}, and Y_{ox} = mass fractions of products, fuel, and oxidizer
Z_i, Z_{ox}, and Z_{fu} = the elemental mass fraction of ith element, oxidizer, and fuel
$\rho\mathbf{g}$ = the gravitational body force

Greek Symbols

ε = the kinetic energy dissipation rate
ε_w = refractory wall emissivity
κ = the absorption coefficient of the medium
κ_B = the Boltzmann constant
λ = the wavelength
μ = laminar absolute viscosity
μ_t = turbulent absolute viscosity
ρ = density
σ_k = turbulent Prandtl number for turbulent kinetic energy
σ_t = constant for the presumed PDF method
σ_s = the scattering coefficient of the medium
σ_ε = turbulent Prandtl number for the kinetic energy dissipation rate
$\bar{\bar{\tau}}$ = the stress tensor
ϕ = equivalence ratio

Appendix

In the RSM, according to the fit of a polynomial equation as expressed in Eq. (A1), a collection of mathematical and statistical techniques are applied. A linear fit is chosen for all the responses. However, if the curvature effect is found to be statistically significant, then a quadratic model needs to be considered instead of a linear one. It should be noted that for the center point case run 33, all the factors are at zero and are used to check the quadratic effect for each run

$$y = \underbrace{\beta_0}_{Mean} + \underbrace{\sum_{i=1}^{k}\beta_i x_i}_{One\ way\ terms} + \underbrace{\sum_{\substack{j=1\\ j<i}}^{k}\sum_{i=1}^{k}\beta_{ij}x_i x_j}_{Two\ way\ intraction\ terms} + \underbrace{h.o.t.}_{Model\ error} + \underbrace{\varepsilon}_{Residualerror} \tag{A1}$$

The impact of each factor on different responses is dissimilar. We need to perform a hypothesis test for the average response through ANOVA, to test if the change in one of the levels or their interaction is significant. Table 4 summarizes the sum of the square parameters required for the ANOVA test. $\bar{y}_i$ is the difference in averaged response for changing factor "A," and similarly, it can be seen for the factor "B," the interaction parameter "AB" and the grand mean.

Analysis of variance parameters are presented in Table 5, for two factors, two levels full factorial design, and the same settings can be expanded for five factors as well. The expression for the total sum of squares can be mathematically written as in Eq. (A2).

It can be remarked that the expression is merely the sum of all the other four entries in that particular column

$$\begin{aligned} SS_T &= \sum_{i=1}^{a}\sum_{j=1}^{b}\sum_{k=1}^{n}(y_{ijk} - \bar{\bar{y}})^2 \\ &= bn\sum_{i=1}^{a}(\bar{y}_i - \bar{\bar{y}})^2 + an\sum_{j=1}^{b}(\bar{y}_j - \bar{\bar{y}})^2 \\ &\quad + n\sum_{i=1}^{a}\sum_{j=1}^{b}(\bar{y}_{ij} - \bar{y}_i - \bar{y}_j - \bar{\bar{y}})^2 + \sum_{i=1}^{a}\sum_{j=1}^{b}\sum_{k=1}^{n}(y_{ijk} - \bar{y}_{ij})^2 \end{aligned} \tag{A2}$$

$$SS_T = SS_{Treatment\,A} + SS_{Treatment\,B} + SS_{InteractionAB} + SS_{Error}$$

$$abn - 1 = a - 1 + b - 1 + (a-1)(b-1) + ab(n-1)$$

As presented in Table 5, for $F > F_0$, that specific main effect or the interaction is considered to be significant. F_0 can be found from the table based on the degrees-of-freedom for each term.

References

[1] Oumarou, N., Kocaefe, D., Kocaefe, Y., and Morais, B., 2016, "Transient Process Model of Open Anode Baking Furnace," Appl. Therm. Eng., **107**, pp. 1253–1260.

[2] Oumarou, N., Kocaefe, D., and Kocaefe, Y., 2018, "An Advanced Dynamic Process Model for Industrial Horizontal Anode Baking Furnace," Appl. Math. Model., **53**, pp. 384–399.
[3] Tajik, A. R., Shamim, T., Ghoniem, A. F., and Abu Al-Rub, R. K., 2019, "Multi-Objective Optimization of Aluminum Anode Baking Process Employing a Response Surface Methodology," Energy Procedia, **158**, pp. 5541–5550.
[4] Kocaefe, Y., Oumarou, N., Baiteche, M., Kocaefe, D., Morais, B., and Gagnon, M., 2013, "Use of Mathematical Modelling to Study the Behavior of a Horizontal Anode Baking Furnace," Light Met., pp. 1139–1144.
[5] Severo, D. S., Gusberti, V., and Pinto, E. C., 2005, "Advanced 3D Modelling for Anode Baking Furnaces," Light Met., pp. 697–702.
[6] Tajik, A. R., Shamim, T., Ghoniem, A. F., and Abu Al-Rub, R. K., 2019, "Optimizing Pulse Combustion Parameters in Carbon Anode Baking Furnaces for Aluminum Production," ASME International Mechanical Engineering Congress and Exposition, Salt Lake City, UT, Nov. 11–14, Vol. 59452, p. V008T09A017.
[7] Tajik, A. R., Zaidani, M., Shamim, T., and Abu Al-Rub, R. K., 2019, "Investigating Effects of Different Flue-Wall Deformation Modes on the Performance of Anode Baking Furnaces for Aluminum Electrolysis," ASME International Mechanical Engineering Congress and Exposition, Salt Lake City, UT, Nov. 11–14, Vol. 59452, p. V008T09A058.
[8] Zaidani, M., Abu Al-Rub, R. K., Tajik, A. R., and Shamim, T., 2017, "Computational Modeling of the Effect of Flue-Wall Deformation on the Carbon Anode Quality for Aluminum Production," ASME 2017 Heat Transfer Summer Conference, Washington, DC, July 9–12, Vol. 57885, p. V001T02A010.
[9] Severo, D. S., Gusberti, V., Sulger, P. O., Keller, F., and Meier, M. W., 2011, "Recent Developments in Anode Baking Furnace Design," Light Met., pp. 853–858.
[10] Tajik, A. R., Shamim, T., Zaidani, M., and Abu Al-Rub, R. K., 2018, "The Effects of Flue-Wall Design Modifications on Combustion and Flow Characteristics of an Aluminum Anode Baking Furnace-CFD Modeling," Appl. Energy, **230**, pp. 207–219.
[11] Tajik, A. R., Shamim, T., Abu Al-Rub, R. K., and Zaidani, M., 2017, "Two Dimensional CFD Simulations of a Flue-Wall in the Anode Baking Furnace for Aluminum Production," Energy Procedia, **105**, pp. 5134–5139.
[12] Tajik, A. R., Abu Al-Rub, R. K., Zaidani, M., and Shamim, T., 2017, "Numerical Investigation of Turbulent Diffusion Flame in the Aluminum Anode Baking Furnace Employing Presumed PDF," Energy Procedia, **142**, pp. 4157–4162.
[13] Zaidani, M., Abu Al-Rub, R. K., Tajik, A. R., and Shamim, T., 2017, "3D Multiphysics Model of the Effect of Flue-Wall Deformation on the Anode Baking Homogeneity in Horizontal Flue Carbon Furnace," Energy Procedia, **142**, pp. 3982–3989.
[14] Zaidani, M., Abu Al-Rub, R. K., Tajik, A. R., and Shamim, T., 2017, "Investigation of the Flue-Wall Aging Effects on the Anode Baking Furnace Performance," ICTEA: International Conference on Thermal Engineering, Muscat, Oman, Feb. 26–28, Vol. 2017.
[15] Zaidani, M., Abu Al-Rub, R. K., Tajik, A. R., Shamim, T., and Qureshi, Z. A., 2017, "The Influence of Flue Wall Deformation on Anode Baking Homogeneity for the Aluminum Production," The 35th International ICSOBA Conference, Hamburg, Germany, Oct. 2–5, pp. 685–698.
[16] Zaidani, M., Tajik, A. R., Qureshi, Z. A., Shamim, T., and Abu Al-Rub, R. K., 2018, "Investigating the Flue-Wall Deformation Effects on Performance Characteristics of an Open-Top Aluminum Anode Baking Furnace," Appl. Energy, **231**, pp. 1033–1049.
[17] Pryor, O., Barak, S., Lopez, J., Ninnemann, E., Koroglu, B., Nash, L., and Vasu, S., 2017, "High Pressure Shock Tube Ignition Delay Time Measurements During Oxy-Methane Combustion With High Levels of CO_2 Dilution," ASME J. Energy Resour. Technol., **139**(4), p. 042208.
[18] Nieckele, A. O., Naccache, M.FN, and Gomes, M. S., 2004, "Numerical Modeling of an Industrial Aluminum Melting Furnace," ASME J. Energy Resour. Technol., **126**(1), pp. 72–81.
[19] Manikantachari, K., Vesely, L., Martin, S., Bobren-Diaz, J. O., and Vasu, S., 2018, "Reduced Chemical Kinetic Mechanisms for Oxy/Methane Supercritical CO_2 Combustor Simulations," ASME J. Energy Resour. Technol., **140**(9), p. 092202.
[20] Almansour, B., Thompson, L., Lopez, J., Barari, G., and Vasu, S. S., 2016, "Laser Ignition and Flame Speed Measurements in Oxy-Methane Mixtures Diluted With CO_2," ASME J. Energy Resour. Technol., **138**(3), p. 032201.
[21] Ghoniem, A. F., Zhao, Z., and Dimitrakopoulos, G., 2019, "Gas Oxy Combustion and Conversion Technologies for Low Carbon Energy: Fundamentals, Modeling and Reactors," Proc. Combust. Inst., **37**(1), pp. 33–56.
[22] Cavaliere, A., and de Joannon, M., 2004, "Mild Combustion," Progress Energy Combust. Sci., **30**(4), pp. 329–366.
[23] Kruse, S., Kerschgens, B., Berger, L., Varea, E., and Pitsch, H., 2015, "Experimental and Numerical Study of MILD Combustion for Gas Turbine Applications," Appl. Energy, **148**, pp. 456–465.
[24] Li, P., Mi, J., Dally, B., Wang, F., Wang, L., Liu, Z., Chen, S., Zheng, C., 2011, "Progress and Recent Trend in MILD Combustion," Sci. China Technol. Sci., **54**(2), pp. 255–269.
[25] Liu, R., and An, E., 2017, "Turbulent Flame Characteristics of Oxycoal MILD Combustion," ASME J. Energy Resour. Technol., **139**(6), p. 062206.
[26] Moghadasi, M. H., Riazi, R., Tabejamaat, S., and Mardani, A., 2019, "Effects of Preheating and CO_2 Dilution on Oxy-MILD Combustion of Natural Gas," ASME J. Energy Resour. Technol., **141**(12), p. 122002.
[27] Noor, M., Wandel, A. P., and Yusaf, T., 2014, "Effect of Air-Fuel Ratio on Temperature Distribution and Pollutants for Biogas MILD Combustion," Int. J. Automot. Mech. Eng., **10**(1), pp. 1980–1992.
[28] Ye, J., Medwell, P. R., Varea, E., Kruse, S., Dally, B. B., and Pitsch, H. G., 2015, "An Experimental Study on MILD Combustion of Prevaporised Liquid Fuels," Appl. Energy, **151**, pp. 93–101.
[29] Brandvik, T., Wang, Z., Ratvik, A. P., and Grande, T., 2017, *Investigation of Spent Refractory Lining in an Anode Baking Furnace*, Springer International Publishing, Cham.
[30] Dong, W., 2000, *Design of Advanced Industrial Furnaces Using Numerical Modeling Method*, Doctoral dissertation, Royal Institute of Technology, Stockholm, Sweden.
[31] Graça, M., Duarte, A., Coelho, P. J., and Costa, M., 2013, "Numerical Simulation of a Reversed Flow Small-Scale Combustor," Fuel Process. Technol., **107**, pp. 126–137.
[32] Galletti, C., Parente, A., and Tognotti, L., 2007, "Numerical and Experimental Investigation of a Mild Combustion Burner," Combust. Flame, **151**(4), pp. 649–664.
[33] Sivathanu, Y., and Faeth, G. M., 1990, "Generalized State Relationships for Scalar Properties in Nonpremixed Hydrocarbon/Air Flames," Combust. Flame, **82**(2), pp. 211–230.
[34] Jones, W., and Whitelaw, J., 1982, "Calculation Methods for Reacting Turbulent Flows: A Review," Combust. Flame, **48**, pp. 1–26.
[35] Ihme, M., and Pitsch, H., 2008, "Prediction of Extinction and Reignition in Nonpremixed Turbulent Flames Using a Flamelet/Progress Variable Model: 2. Application in LES of Sandia Flames D and E," Combust. Flame, **155**(1), pp. 90–107.
[36] Ihme, M., and Pitsch, H., 2008, "Prediction of Extinction and Reignition in Nonpremixed Turbulent Flames Using a Flamelet/Progress Variable Model: 1. A Priori Study and Presumed PDF Closure," Combust. Flame, **155**(1), pp. 70–89.
[37] Cao, H.-J., Zhang, H.-Q., and Lin, W.-Y., 2012, "Evaluation of Presumed Probability-Density-Function Models in Non-Premixed Flames by Using Large Eddy Simulation," Chin. Phys. Lett., **29**(5), p. 054705.
[38] Kulkarni, R., and Polifke, W., 2012, "Large Eddy Simulation of Autoignition in a Turbulent Hydrogen Jet Flame Using a Progress Variable Approach," J. Combust., **2012**, pp. 1–11.
[39] Jiang, Q., Zhang, C., and Jiang, J., 2004, "Reduction of NO_x in a Regenerative Industrial Furnace With the Addition of Methanol in the Fuel," ASME J. Energy Resour. Technol., **126**(2), pp. 159–165.
[40] Ishii, T., Zhang, C., and Sugiyama, S., 2000, "Effects of NO Models on the Prediction of NO Formation in a Regenerative Furnace," ASME J. Energy Resour. Technol., **122**(4), pp. 224–228.
[41] Ishii, T., Zhang, C., and Sugiyama, S., 1998, "Numerical Simulations of Highly Preheated Air Combustion in an Industrial Furnace," ASME J. Energy Resour. Technol., **120**(4), pp. 276–284.
[42] Ansys, I., 2011, *ANSYS FLUENT Theory Guide*, ANSYS Inc., Canonsburg, PA, p. 794.
[43] Zhang, J., Liang, Y., and Harpalani, S., 2016, "Optimization of Methane Production From Bituminous Coal Through Biogasification," Appl. Energy, **183**, pp. 31–42.
[44] Thummakul, T., Gidaspow, D., Piumsomboon, P., and Chalermsinsuwan, B., 2017, "CFD Simulation of CO_2 Sorption on K_2CO_3 Solid Sorbent in Novel High Flux Circulating-Turbulent Fluidized Bed Riser: Parametric Statistical Experimental Design Study," Appl. Energy, **190**, pp. 122–134.
[45] Naqiuddin, N. H., Saw, L. H., Yew, M. C., Yusof, F., Poon, H. M., Cai, Z., and Thiam, H. S., 2018, "Numerical Investigation for Optimizing Segmented Micro-Channel Heat Sink by Taguchi-Grey Method," Appl. Energy, **222**, pp. 437–450.
[46] Shirvan K, M., Mirzakhanlari, S., Mamourian, M., and Kalogirou, S. A., 2017, "Optimization of Effective Parameters on Solar Updraft Tower to Achieve Potential Maximum Power Output: A Sensitivity Analysis and Numerical Simulation," Appl. Energy, **195**, pp. 725–737.
[47] Bahai, H., Esat, I., and Rass, L., 1995, "A Factorial Design Approach to Investigate the Effect of Geometry in Drill String Screw Connectors?" ASME J. Energy Resour. Technol., **117**(2), pp. 101–107.
[48] Brookes, S. J., and Moss, J. B., 1999, "Measurements of Soot Production and Thermal Radiation From Confined Turbulent Jet Diffusion Flames of Methane," Combust. Flame, **116**(1), pp. 49–61.
[49] Yang, X., He, Z., Dong, S., and Tan, H., 2018, "Prediction of Turbulence Radiation Interactions of CH_4H_2/Air Turbulent Flames at Atmospheric and Elevated Pressures," Int. J. Hydrogen Energy, **43**(32), pp. 15537–15550.